Isotropic 3D electron microscopy reference library of whole cells and tissues

C. Shan Xu[1]†, Song Pang[1]*, Gleb Shtengel[1]*, Andreas Müller[2,3,4], Alex T. Ritter[5], Huxley K. Hoffman[6#], Shin-ya Takemura[1], Zhiyuan Lu[1], H. Amalia Pasolli[1§], Nirmala Iyer[1], Jeeyun Chung[7,8], Davis Bennett[1], Aubrey V. Weigel[1], Tobias C. Walther[7,8,9], Robert V. Farese, Jr.[7,8], Schuyler B. van Engelenburg[6], Ira Mellman[5], Michele Solimena[2,3,4,10], Harald F. Hess[1]†

Affiliations

[1]Janelia Research Campus, Howard Hughes Medical Institute, Ashburn, VA 20147, USA

[2]Molecular Diabetology, University Hospital and Faculty of Medicine Carl Gustav Carus, TU Dresden, Dresden, Germany

[3]Paul Langerhans Institute Dresden (PLID) of the Helmholtz Center Munich at the University Hospital Carl Gustav Carus and Faculty of Medicine of the TU Dresden, Dresden, Germany

[4]German Center for Diabetes Research (DZD e.V.), Neuherberg, Germany

[5]Genentech, Inc., 1 DNA Way, South San Francisco, CA 94080, USA

[6]Molecular and Cellular Biophysics Program, Department of Biological Sciences, University of Denver, Denver, CO 80210, USA

19 [7]Department of Molecular Metabolism, Harvard T.H. Chan School of Public Health, Boston, MA

20 02115, USA

21 [8]Department of Cell Biology, Harvard Medical School, Boston, MA 02115, USA

22 [9]Howard Hughes Medical Institute, Boston, MA 02492, USA; Broad Institute of Harvard and

23 MIT, Cambridge, MA 02124, USA

24 [10]Max-Planck Institute of Molecular Cell Biology and Genetics, Dresden, Germany

25 †Correspondence to: xuc@janelia.hhmi.org (C.S.X), hessh@janelia.hhmi.org (H.F.H.)

26 *These authors contributed equally to this work

27 [#]Present Address: Department of Cell and Developmental Biology, University of Colorado

28 Anschutz Medical Campus, Aurora, CO 80045, USA

29 [§]Present Address: Electron Microscopy Resource Center, The Rockefeller University, New York,

30 NY 10065, USA

Summary

Understanding cellular architecture is essential for understanding biology. Electron microscopy (EM) uniquely visualizes cellular structure with nanometer resolution. However, traditional methods, such as thin-section EM or EM tomography, have limitations inasmuch as they only visualize a single slice or a relatively small volume of the cell, respectively. Here, we overcome these limitations by imaging whole cells and tissues with enhanced Focus Ion Beam Scanning Electron Microscopy (FIB-SEM) in high resolution with month-long acquisition duration. We use this approach to generate reference 3D image datasets at 4-nm isotropic voxels for ten different examples, including cultured cells (cancer, macrophages, and T-cells) as well as tissues (mouse pancreatic islets and the *Drosophila* fan-shaped body). We open access to all datasets in OpenOrganelle, an interactive web platform that allows accessing both the original 3D EM data, and subsequent organelle segmentation. Together, these data will serve as a reference library to explore comprehensive quantification of whole cells and their constituents, thus addressing questions related to cell identities, cell morphologies, cell-cell interactions, as well as intracellular organelle organization and structure.

Main

Individual cells and organized systems of cells within a tissue can be described with a hierarchy of ultrastructural details, from complex organelle networks down to single protein molecules[1]. While transmission electron microscopy (TEM) and scanning electron microscopy (SEM) images from diamond-knife cut thin sections of metal stained samples have profoundly shaped our understanding of organelles[2], such approaches generate 2D images that can reveal 3D

52 structures, but may be limited due to constraints from the section thickness (of ~30–300 nm),
53 allowing only a small fraction of the whole cell to be captured. Furthermore, that sampled
54 fraction is often viewed at a specific sectioning angle through the cell or tissue, limiting visibility
55 of many structural aspects unless many sections are examined. Series of sections can be
56 digitally stitched together to form a 3D volume, but the 30 nm or larger sampling interval from
57 section to section sacrifices much structural detail. Tilt tomography can overcome this problem
58 but is confined in volume size to ~ 100 μm^3. Stitching together data of multiple such sections
59 can extend the effective volume size but is arduous and currently not practical for more than a
60 dozen sections. Alternatively, diamond-knife cut surfaces of a block face sequentially imaged
61 with SEM[3] was a pioneering step to access larger volumes, but its z resolution is limited to 25
62 nm due to electron radiation damage to the block face from beam scanning that prevents
63 consistent cutting of thinner slices[4]. Thus, high-resolution isotropic 3D whole cell data remain
64 mostly out of reach.

65 The constraints of diamond-knife cutting thickness can be removed by using a focused
66 ion-beam, typically of gallium ions, to abrade arbitrarily fine increments of the block surface as
67 thin as 1 nm. This technique, combined with SEM, is called FIB-SEM. Here, we advance FIB-SEM
68 with a 90° angle between the imaging electron beam and the milling ion beam (Fig. 1a), along
69 with other modifications to transform conventional FIB-SEM that is lacking of long-term
70 reliability to an enhanced platform that is capable of months to years of continuous imaging
71 without defects in the final image stack[5,6,7]. We further systematically optimized both ion
72 milling and electron imaging components to achieve 4-nm sampling intervals in all three
73 dimensions, thus enabling high-resolution imaging by rendering greater details with volumes

74 approaching (100 µm)^3. The ability of enhanced FIB-SEM to image whole cells and tissues at 4-
75 nm isotropic voxels over large volumes makes it an ideal tool to map *in toto* the 3D
76 ultrastructural relationship of organelles and protein complexes in living systems. The resulting
77 data are unique in their size and level of 3D detail, and are presented for a variety of cells and
78 tissues to establish a reference library of cellular architecture.

79 Finer Resolution

80 With the dual biological motivations to image with fine resolution *and* encompass the largest
81 possible volumes, we confront limitations and tradeoffs between these two goals. The isotropic
82 resolution limits are convoluted by 1) the waist size of the incoming primary electron beam,
83 and 2) the size of the scattering volume explored by the penetrating primary electrons. To
84 optimize for point 1, the best beam focus, spherical and chromatic aberrations of the
85 electromagnetic lenses can be mitigated by operating at modest numerical aperture through
86 smaller beam currents hence achieving the best x-y resolution. For point 2, lower primary beam
87 landing energy generates fewer scattering events, resulting in smaller scattering volume which
88 improves resolutions along all three axes. Any further reduction below the optimal energy will
89 result in a reduced scattering ratio of the heavy metal stain atoms over lighter background
90 atoms of the sample resin, thus fading contrast.

91 Through investigating a multi-dimensional parameter space, we found that a beam
92 current of 200 to 300 pA and a landing energy of 700 to 900 eV are optimal for isotropic 4 nm
93 imaging. To characterize the resolution in x-y and z, we analyzed the step transitions at the
94 edges of gold nano particles on a carbon substrate. The vertical lines in Fig. 1b indicate an x-y

95 transition distance of 2.0 nm for SEM signal change from 37% to 63%, or of 5.5 nm for
96 transition from 20% to 80%. One can use ribosomes in a similar way as an *in situ* resolution
97 standard to get the full 3D edge transition. The ribosome x-y transitions are about 30% larger
98 than the gold nano particle x-y edges, probably from it being a non-ideal step edge. As an
99 alternative conservative measure of resolution, this corresponds 12 nm Gaussian full width half
100 maximum (FWHM) in x-y plane. In addition, Fig. 1b shows mostly isotropic resolution on a
101 number of different samples where the z transitions are 30% larger than the x-y edge
102 transitions. The procedure for estimating the resolution and some examples are presented in
103 Methods Section.

104 Larger Volumes

105 Large volumes are crucial to study biology, driven by demands of completeness and sufficient
106 statistics. In acquiring the largest possible volumes with the finest resolution, we allocate 6,000
107 to 10,000 electrons per voxel (depending on sample contrast) to achieve a target contrast
108 (between membrane and resin) to shot noise ratio of three or higher. This translates to a
109 sampling rate of < 200 kHz (dwell time > 5 µs) needed with a 200-pA primary beam. We set the
110 sampling voxel size to 4 nm to be consistent with the resolution determined from edge
111 transitions. These values define a volumetric imaging rate of < $(10\ \mu m)^3$/day. The continuous
112 operating duration of conventional FIB-SEM systems is constrained to ~3 days, which inevitably
113 caps the maximum possible 3D volume to $(\sim 15\ \mu m)^3$.

114 To access volumes of typical whole cells either in culture or in tissue, reliable long-term
115 imaging approaching one month with nanometer stability is required. This is particularly

116 challenging when the highest resolution and the largest possible volumes are desired. Fig. 1c,
117 places this capability in context of other existing 3D EM methods where bottom axis is sample
118 size and vertical axis is isotropic voxel size. Note that to access very large volumes such as the
119 whole *Drosophila* brain of $40x10^6$ μm^3, a higher current with lower resolution of 8 nm voxels
120 was used (Fig. 1c). The enhanced FIB-SEM technology, initially motived by the *Drosophila*
121 connectome project[8] and demonstrated preliminary value to cell biology[9], delivers continuous
122 stable and reliable operation for months to years, which is also optimized for fine resolution
123 whole cell imaging.

124 Open Data

125 Access to this new region of large volumes with high resolution imaging requires a considerable
126 investment in technology development, equipment resources, and imaging duration, but the
127 resulting wealth of data is unique and comprehensive, covering whole cells with all their
128 organelles and proteins that can be highlighted with heavy metal stains. Here, we provide ten
129 such datasets containing seven common wild-type cultured cell samples and three different
130 tissue samples. To enable the wider scientific community to browse, download, and explore, we
131 open access the data via OpenOrganelle (https://openorganelle.janelia.org)[10]. For each sample,
132 metadata and pre-selected views of interest are provided, while cross-sections can be explored
133 with *neuroglancer*, a built-in visualization tool. This repository also includes further processing,
134 such as segmentation to categories of interest[10], which forms a basis for quantifying numbers,
135 sizes, shapes, contacts, locations, proximity or any other parameters and distributions of EM
136 stained organelles and proteins in the whole cell. While these datasets will serve as the starting

137 point of a reference library to explore comprehensive cellular architecture, we hope to further
138 extend such reference datasets to yet other cells and tissues.

139 Discussion of Exemplary Samples

140 The initial datasets of seven common wild-type cultured cells and three tissue samples are
141 tabulated in Table 1. The cells have been cryo-fixed by high pressure freezing (HPF), which
142 vitrifies a sample on a millisecond time scale to best preserve any dynamic structural details.
143 This also minimizes any possibility of artifacts that might be of concern with chemical fixation.
144 The subsequent freeze substitution labels biomolecules with heavy metals to provide contrast
145 for EM. While thin tissue samples (< 200-µm-thick) can be similarly cryo-fixed, in many cases
146 thick tissue specimens cannot be cryo-fixed (e.g., large brain tissue) thus requiring various
147 chemical fixation and staining protocols. We also offer a selection of these tissue samples as
148 initial reference datasets. The 3D images all used 4 nm voxels sampled at rates of 100 kHz – 2
149 MHz with ~ 250 pA of primary beam current. The samples with stronger staining were imaged
150 at much faster rates while maintaining similar image quality. The time to acquire these volumes
151 ranged from 2 weeks to 5 weeks of uninterrupted imaging.

152 Individual HeLa Cell

153 **HeLa cells**, human cervical cancer cells, are easily cultured and widely used in cell biology
154 laboratories as a basic model to test diverse hypotheses. Having such cells imaged in their
155 entirety can provide a reference to which perturbations in growth, genetic, environment, etc.
156 can be compared. Fig. 2 presents a typical 200 GB 3D dataset on the example of an entire HeLa
157 cell. The mitochondrial network is shown in green. The bottom row panels show 2D cross-

158 sections of standard cellular organelles, such as the centrosome (Fig. 2b), the Golgi apparatus
159 (Fig. 2c), and nuclear envelope (Fig. 2d). Notably, every example illustrates the advantages of
160 isotropic 3D imaging for cell biology. No single 2D cross-section allows visualizing all centriole
161 sub-distal appendages, however quick segmentation of the 3D dataset shows them clearly (red,
162 Fig. 2b). Stereotypical 2D images of the Golgi stacks do not reveal the fenestration details and
163 long thin tubular extensions, that can only be seen in 3D (magenta – single segmented Golgi
164 cisterna – Fig. 2c). Polyribosomal chains on the nuclear envelope are mostly hidden in 2D cross-
165 sections but easily resolved and detailed in 3D (Fig. 2d).

166 Interacting Cell Pairs: T Cell Attacking Cancer

167 **Cytotoxic T lymphocytes** (CTLs) are immune cells that have the capacity to identify and destroy
168 virus-infected or cancerous cells. Upon encountering a target, CTLs undergo a dramatic
169 cytoskeletal rearrangement to form an organized intercellular interface called the
170 immunological synapse (IS). Signaling at the IS directs the polarized release of toxic proteins
171 housed in specialized secretory lysosomes called lytic granules (LGs), which results in target cell
172 death. Due to the important role of CTLs in anti-viral and anti-cancer immunity, the IS has been
173 the subject of intense scrutiny. Many studies of the IS have been performed on artificial planar
174 lipid bilayers created on glass coverslips. These synthetic two-dimensional surfaces lack the
175 complex receptor content and membrane topology of a real cancer cell. Studies of IS formation
176 between actual cells, although more challenging, present more biologically relevant content.
177 Limited single slice TEM images of CTL:target conjugates have revealed interesting features of
178 the IS, but do not represent the full scope of this dynamic, three-dimensional structure[11]. Fig.
179 3a presents a 1.4-TB 3D dataset (16bit) of a mature murine CTL (green) engaging an ID8 ovarian

180 cancer cell (cyan). The isotropic high-resolution information of FIB-SEM imaging provides a
181 unique and complete map of the complex membrane topology at the interface between T cell
182 and target. Fig. 3b shows one cross section demonstrating the stereotypical CTL "cupping" of
183 the target cell at the IS. Zoomed in images show the variety of features across this interface
184 including membrane interdigitation (Extended Data Fig. 1a), flat membrane apposition
185 (Extended Data Fig. 1b), and filopodia of the target cell trapped between the two cells
186 (Extended Data Fig. 1c). Without the ability to scan in 3D, these filopodia may be mistaken for
187 vesicles trapped between T cell and target.

188 Another hallmark of CTL killing is the polarization of the centrosome toward the target
189 cell[12,13], which can be observed in Fig. 3c. FIB-SEM allows for the label-free localization of all
190 organelles in the T cell including those responsible for target killing and cytokine secretion.
191 Individual 2D EM slices may miss the Golgi stacks and lytic granules (Fig. 3d) which can be found
192 by scanning the FIB-SEM volume around the centrosome.

193 Tissues: Mouse Pancreatic Islets and *Drosophila* Brain Fan-shaped Body

194 **Pancreatic islets** are micro-organs consisting mainly of beta, alpha, delta, polypeptide cells and
195 endothelial cells. Among them beta cells are in the majority and secrete insulin stored in
196 secretory granules (SGs) to maintain blood glucose homeostasis. Beta cells have a polyhedral
197 shape with a longer axis that can easily reach 20 µm[14], posing significant challenges for high
198 resolution whole cell imaging. Few beta cells have been reconstructed by serial section electron
199 tomography at medium resolution[15] to allow assessment of subcellular features such as insulin
200 SG number and shape of mitochondria, but lacking the resolution for imaging of e.g., ER and
201 microtubules. Large-scale high-resolution FIB-SEM enables the analysis of ultrastructural

202 differences between beta cells within an islet as well as features that require higher resolution
203 such as ribosomes and the cytoskeleton. In our studies, especially the preservation of
204 cytoskeletal elements benefits from fixation by HPF. Fig. 4a displays a 200-GB volume with
205 several complete beta cells that are entirely included within the 30 x 20 x 25 μm^3 volume. The
206 large field of view allows for imaging the interaction of beta cells, e.g., full primary cilia and
207 their connections to neighboring cells and the intermingling of microvilli (Fig. 4b and 4c). At 4-
208 nm voxel sampling, we observed ultrastructural differences between insulin SGs (Fig. 4d). For
209 the first time, we report close contacts of ER and insulin SGs in 3D (Fig. 4e). Ultimately, such
210 high resolution allows the sharp definition of microtubules, single ribosomes and Golgi stacks
211 for quantitative measurements (Fig. 4f). The seamless imaging results in precisely aligned stacks
212 furthermore facilitating automated 3D segmentation. Specifically, from these FIB-SEM datasets
213 has emerged a comprehensive 3D representation of microtubule networks and how they
214 interact with other organelles[16]. We could show that beta cell microtubules are arranged into
215 non-radial networks which for the most part do not originate either from centrioles or
216 endomembranes. Furthermore, glucose stimulation changes the number and length of
217 microtubule polymers without changing their overall density. Finally, we found insulin SGs to be
218 enriched near the plasma in association with microtubules, independent of the extracellular
219 glucose levels.

220 The **central complex in insect brains** is a highly conserved brain region that controls
221 various behaviors. Fig. 4g shows higher-resolution images acquired from the fan-shaped body
222 of the central complex of the fruit fly, *Drosophila*. For a detailed understanding of brain
223 functions, it is imperative to identify the synaptic levels of neuron connectivity through key

224 synaptic elements such as presynaptic T-bars and postsynaptic densities (PSDs) (Fig. 4i, 4j). To
225 investigate if the central complex contains characteristic synaptic motifs, such as polyadic
226 synapse, rosette synapse, or any new synaptic motif, validating the synaptic structures with
227 high-resolution images is crucial. However, often a trade-off between imaging a large volume
228 with low-resolution and acquiring high-resolution with a small volume limits answering
229 questions in connectomics, where fine synaptic structure identification and large-scale
230 neuronal tracing are equally important. Higher resolution FIB-SEM images with large volume
231 therefore provide significant values to the study. Such datasets allow reconstruction of not only
232 the large neuronal objects and glial cells, but also smaller intracellular components such as
233 synaptic vesicles, dense-core vesicles (Fig. 4h), and microtubules (Fig. 4k, 4l). Knowing the types
234 of synaptic vesicles could add important insights to the understanding of the properties of
235 synaptic connections. As an example, the terminals of dopaminergic neurons in the fly's
236 olfactory center were shown to contain both clear and dense-core vesicles[17], in congruence
237 with having more than one neurotransmitter[18].

238 Summary

239 While three-dimensional imaging offers tremendous value to elucidate biological structures and
240 decipher their function, the enhanced FIB-SEM platform has advanced to image not only partial
241 but entire mammalian cells or multicellular parts of tissues at 4-nm isotropic voxels, hence
242 revealing a more holistic 3D ultrastructural picture in living systems. We have imaged a variety
243 of biological samples over volumes of $(100\ \mu m)^3$ to study the complex morphologies of cells, the
244 complete interfaces involved in cell-cell interactions, and the shapes, volumes, distributions,

245 and relationships of intracellular organelles. This has allowed for new biological insights. For
246 example, the datasets of mouse pancreatic islets (Fig. 4a–4f) unveil a comprehensive 3D
247 representation of the microtubule network and how it interacts with other organelles, as well
248 as microtubule remodeling as a result of glucose stimulation[16]. Likewise, the data of HeLa and
249 U2-OS nuclei were mined to identify and characterize chromatin domains[19]. In a similar spirit,
250 we feel that guided by other research questions, many insights can be gleaned from this raw
251 data through customized analysis.

252 As we envision many fruitful discoveries to be enabled via access to the 3D data in the
253 larger context of cells in tissues, we aim to expand our portfolio on OpenOrganelle[10] to include
254 other tissues. The initial datasets of various healthy wild-type cells, can be explored to define
255 reference features of interest, such as microtubule proximity to certain vesicles, or ER
256 morphology near a particular organelle or ribosome chain length on curved ER near the Golgi
257 apparatus. The possibilities seem limitless and are actually daunting. Open access preview on a
258 wild-type healthy cell can encourage further experiments to compare such features against
259 perturbations of disease, mutations, development, or environment. Whole cell structural
260 differences can be quantified and measured against these perturbations. In additional to target
261 feature analysis, unanticipated new features could also be discovered. Segmentation is a crucial
262 next step to aid biologists in such analysis. However, the semi-manual attempt on a HeLa cell
263 (Fig. 2) is time-consuming. A more rapid approach needed on the whole cell scale is presented
264 in the associated paper[10]. We believe that open access to rich 3D FIB-SEM datasets will provide
265 important insights, guidance, and inspiration for further exploration to the research community
266 to address a new broad range of biological questions.

267

Reference

[1] Lodish H. et al. *Molecular Cell Biology* (W. H. Freeman, New York, 2016).

[2] Porter, K. R., Claude, A., & Fullam, E. F. A study of tissue culture cells by electron microscopy: methods and preliminary observations. *The Journal of experimental medicine*, **81**(3), 233–246 (1945). https://doi.org/10.1084/jem.81.3.233

[3] Denk W., & Horstmann H. Serial block-face scanning electron microscopy to reconstruct three-dimensional tissue nanostructure. *PLoS Biol* 2004, **2**:e329 (2004). https://doi.org/10.1371/journal.pbio.0020329

[4] Titze B. Techniques to prevent sample surface charging and reduce beam damage effects for SBEM imaging. Dissertation. Heidelberg University. 1–112 (2013). https://doi.org/10.11588/heidok.00015372

[5] Xu C. S. et al. Enhanced FIB-SEM systems for large-volume 3D imaging. *eLife* **6**:e25916 (2017). https://doi.org/10.7554/eLife.25916

[6] Xu, C. S., Hayworth K. J., & Hess H. F. Enhanced FIB-SEM systems for large-volume 3D imaging. US Patent 10,600,615, 24 Mar (2020).

[7] Xu C. S., Pang S., Hayworth K. J., & Hess H. F. Transforming FIB-SEM Systems for Large-Volume Connectomics and Cell Biology. In: Wacker I., Hummel E., Burgold S., Schröder R. (eds) Volume Microscopy. Neuromethods, vol 155 (2020). Humana, New York, NY. https://doi.org/10.1007/978-1-0716-0691-9_12

[8] Xu C. S. et al. A connectome of the adult *Drosophila* central brain. *bioRxiv* 2020.01.21.911859. (2020). https://doi.org/10.1101/2020.01.21.911859

[9] Wu, Y. et al. Contacts between the endoplasmic reticulum and other membranes in neurons. *PNAS* **114**(24) E4859-E4867 (2017). https://doi.org/10.1073/pnas.1701078114

[10] Heinrich, L. et al. Automatic whole cell organelle segmentation in volumetric electron microscopy. (2020).

[11] Stinchcombe J. C., Bossi G., Booth S., & Griffiths G. M. The immunological synapse of CTL contains a secretory domain and membrane bridges. *Immunity*. 2001;15(5):751–761. https://doi.org/10.1016/s1074-7613(01)00234-5

[12] Kupfer A. & Dennert G. Reorientation of the microtubule-organizing center and the Golgi apparatus in cloned cytotoxic lymphocytes triggered by binding to lysable target cells. *J Immunol*. 1984;133(5):2762-2766.

[13] Stinchcombe J. C., Majorovits E., Bossi G., Fuller S. & Griffiths G.M. Centrosome polarization delivers secretory granules to the immunological synapse [published correction appears in Nature. 2006 Nov 9;444(7116):236]. *Nature*. 2006;443(7110):462–465. https://doi.org/10.1038/nature05071

[14] Fava, E. et al. Novel standards in the measurement of rat insulin granules combining electron microscopy, high-content image analysis and in silico modelling. *Diabetologia* **55**, 1013–1023 (2012). https://doi.org/10.1007/s00125-011-2438-4

[15] Noske, A. B., Costin, A. J., Morgan, G. P. & Marsh, B. J. Expedited approaches to whole cell electron tomography and organelle mark-up in situ in high-pressure frozen pancreatic islets. *J. Struct. Biol.* **161**, 298–313 (2008). https://doi.org/10.1016/j.jsb.2007.09.015

[16] Müller, A. et al. Three-dimensional FIB-SEM reconstruction of microtubule-organelle interaction in whole primary mouse beta cells. *bioRxiv* 2020.10.07.329268. (2020). https://doi.org/10.1101/2020.10.07.329268

[17] Takemura, S. Y. et al. A connectome of a learning and memory center in the adult *Drosophila* brain. *eLife* **6**, e26975 (2017). https://doi.org/10.7554/eLife.26975

[18] Aso, Y. et al. Nitric oxide acts as a cotransmitter in a subset of dopaminergic neurons to diversify memory dynamics. *eLife* **8**, e49257 (2019). https://doi.org/10.7554/eLife.49257

[19] Miron, E. et al. Chromatin arranges in chains of mesoscale domains with nanoscale functional topography independent of cohesion. *Sci. Adv.*, **6**, 39 eaba8811 (2020). https://doi.org/10.1126/sciadv.aba8811

268

Methods

Cultured cell sample preparation

1. HeLa cells

HeLa cells (CCL-2) were purchased from American Type Culture Collection (ATCC). HeLa cells were maintained in EMEM medium (ATCC, 30-2003) supplemented with 10% FBS (Corning, 35-011-CV) and 1X penicillin-streptomycin solution (Corning, 30-002-CI). Trypsinized HeLa cells were seeded on pre-cleaned and edge-coated sapphire coverslips. Immediately prior to freezing, live cells are inspected to ensure cell morphology and viability. After quality assurance the cells are transferred to a water jacketed CO_2 incubator (ThermoFisher, Midi 40) kept at 37° C, 5% CO_2, and 100% humidity while awaiting freezing. Each coverslip is removed from the incubator immediately prior to the freezing procedure. Cell samples were cryo-fixed using a Wohlwend Compact 2 high-pressure freezer (Engineering Office M. Wohlwend GmbH, Bifig 14, 9466 Sennwald, Switzerland). The BSA mixture is used as a cell cryo-protectant to prevent ice crystal formation in the extra cellular space[20]. Once the sample is frozen it can be stored indefinitely in liquid nitrogen for subsequent freeze-substitution and resin embedding. Freeze-substitution (FS) was performed using automated FS machine (AFS2, Leica Microsystems): coverslips were transferred to cryotubes containing FS media (2% OsO_4, 0.1% Uranyl Acetate (UA), and 3% water in acetone) under liquid nitrogen, followed by a programmed FS schedule. Resin embedding was performed immediately after FS. Samples were removed from the AFS2 machine, washed 3 times in anhydrous acetone for a total of 10 min and embedded in Eponate 12 which was polymerized for 48 hours at 60°C. Following EPON embedding, the coverslip is separated from the resin block containing the cells by sequential immersion in liquid nitrogen

291 and hot water. Once the coverslip is removed, the exposed surface is immediately re-
292 embedded in Durcupan resin which helps minimize streaks during FIB-SEM imaging[5]. The detail
293 procedures of coverslip preparation, high pressure freezing, free substitution, and resin
294 embedding are presented in the Supplementary Information.

295 ## 2. Cytotoxic T cell and T cell/Cancer cell conjugate (CTLs)

296 To generate CTLs from OT-I mice (Jackson Labs), splenocytes were isolated and stimulated with
297 10nM OVA257-264 peptide (AnaSpec, Fremont, CA, USA) in 10% RPMI (RPMI 1640 plus 10%
298 fetal bovine serum (Fisher), 2mM L-glutamine, 50U/mL penicillin/streptomycin, and 50µM β-
299 mercaptoethanol. Following 3 days of stimulation, cells were resuspended in complete media
300 plus 10 IU/mL recombinant human IL-2 (rHIL-2, Roche), and seeded in fresh media at $0.5x10^6$
301 cells/mL every 48 hours. ID8 cancer cell line (ATCC) was grown in RPMI media (Gibco) with 10%
302 FBS (Gibco).

303 In-vitro activated CTLs from Ova-transgenic (OT-I) mice were combined with adherent ID8
304 murine ovarian cancer cells. To facilitate recognition of cancer cells by the OTI-I CTLs, ID8 cells
305 suspended in complete medium (RPMI with 10% FBS, Gibco) were incubated with $OVA_{257-264}$
306 SIINFEKL peptide for 1 hour at 37°C. The cells were washed three times with complete medium,
307 and 10^5 cells were added to each well of a 24-well plate. Each well contained a single sapphire
308 coverslip coated with human Fibronectin (Corning). The ID8 cells were allowed to settle and
309 adhere for 2 hours in an incubator at 37°C/5% CO_2. At this time, the media in the well was
310 replaced with 250uL phenol-red free RPMI (Gibco). Care was taken to ensure that media and
311 cells were stored in 37°C/5% CO_2 for all incubation periods. Immediately after changing the
312 media, 10^5 CTLs in 50uL complete medium were added to the well. The CTLs were allowed 7

313 minutes to find their targets and secrete lytic granules before fixation through high pressure
314 freezing. The relatively short incubation time favors capture of CTL:target conjugates in an
315 early-stage of interaction.

316 The remaining cryofixation, FS, and resin embedding procedures were identical to those
317 described for HeLa cells. The detail procedures are presented in the Supplementary
318 Information.

319 Tissue sample preparation

320 1. Mouse pancreatic islets

321 Pancreatic islets of 9-week-old C57BL/6 mice were isolated as previously described[21]. They
322 were cultured overnight in standard culture media (RPMI 1640 (Gibco) with 10% FBS, 20 mM
323 HEPES, 100 U/ml each penicillin and streptomycin) containing 5.5 mM glucose. Prior to high
324 pressure freezing the islets were subjected to 1 hr incubation in Krebs-Ringer buffer containing
325 either 3.3 mM or 16.7 mM glucose.

326 Islets were frozen with a Leica EM ICE high pressure freezer (Leica Microsystems, Germany)
327 and kept in liquid nitrogen until freeze substitution. They were substituted as previously
328 published[22] or according to a novel protocol: first the samples were substituted in a cocktail
329 containing 2% OsO_4, 1% UA, 0.5% glutaraldehyde, 5% H2O in Acetone with 1% Methanol at -
330 90°C for 24 hours. The temperature was raised to 0°C over 15 hours followed by 4 washes with
331 100% acetone for 15 min each and an increase in temperature to +22°C. Afterwards the
332 samples were incubated in 0.2% thiocarbohydrazide in 80% methanol at RT for 60 min followed
333 by 6 x 10 min washes with 100% acetone. The specimens were stained with 2% OsO_4in acetone
334 at RT for 60 min followed by incubation in 1% UA in acetone + 10% methanol in the dark at RT

335 for 60 min. After 4 washes in acetone for 15 min each they were infiltrated with increasing
336 concentrations of Durcupan resin in acetone followed by incubation in pure Durcupan and
337 polymerization at 60°C. For quality control the blocks were sectioned with a Leica LC6
338 ultramicrotome (Leica microsystems) and 300 nm sections were put on slot grids containing a
339 Formvar film. Tilt series ranging from -63° to +63° were acquired with a F30 electron
340 microscope (Thermo Fisher) and reconstructed with the IMOD software package[23].

341 2. Drosophila brain samples (fan-shaped body and accessory calyx)

342 *Drosophila* brain tissues from 5-day-old adult (Genome type: iso Canton S G1 x w1118 iso 5905)
343 were prepared according to Progressive Lowering of Temperature and Low Temperature
344 Staining (PLT-LTS) heavy metal enhancement protocol described previously[24].
345 In details, after tissue dissection and pre-fixation, we osmicated tissue in 1% OsO_4. This was
346 followed without washing by 1.5% K ferrocyanide, then a complete wash and finally, a transfer
347 for 15 min to 1% thiocarbohydrazide at 22°C, followed in turn by a complete wash then 2%
348 osmium for 30 min at 22°C. After osmication we stained in lead aspartate for 30 min at 55°C,
349 followed by 1 h at 22°C. The tissue was then dehydrated using the PLT method as in Method 3,
350 followed by low temperature en bloc staining in either 0.2% uranyl acetate in acetone, or 1%
351 EPTA in 97% ethanol. Specimens were infiltrated and embedded in Durcupan.

352 Preparation for FIB-SEM

353 After Durcupan re-embedding, a 3D X-Ray tomogram of the entire block is taken using an
354 XRadia-510 Versa micro X-Ray system (Carl Zeiss X-ray Microscopy, Inc.). The 3D X-Ray
355 tomograms allow for selecting Region of Interest (ROI) efficiently. Specifically, it identifies cells
356 with good morphology (for example a properly shaped cell, a cell in a desired stage of mitosis, a

357 T-cell attacking a cancer cell, etc.), and also determines the proper orientation for the tissue
358 samples. Once a potential ROI is identified, the sample block is re-mounted to the top of a 1
359 mm copper post (using Durcupan) which was in contact with the metal-stained sample for
360 better charge dissipation, as previously described[5]. Each sample is oriented on the copper post
361 to allow the shortest distance along FIB milling direction. A small vertical sample post is
362 trimmed to the ROI with a width of ~100 µm and a depth of 60 ~ 80 µm in the direction of the
363 ion beam for each sample. Sample trimming uses an ultramicrotome (EM UC7, Leica
364 Microsystems), is done in few iterations with X-Ray tomogram collected after every step.
365 Once the desired ROI is trimmed, a thin layer of conductive material of 10-nm gold
366 followed by 100-nm carbon was coated on the trimmed samples using a Gatan PECS 682 High-
367 Resolution Ion Beam Coater. The coating parameters were 6 keV, 200 nA on both argon gas
368 plasma sources, 10 rpm sample rotation with 45-degree tilt.

369 ## FIB-SEM imaging

370 A Zeiss Gemini 500-Capella Crossbeam system and Zeiss Merlin crossbeam system[5,6] were
371 further modified for this work in the following ways: the FEI Magnum FIB column was replaced
372 with a Zeiss Capella FIB column; the Zeiss Capella FIB column was repositioned at 90 degrees to
373 the SEM column; and the custom NI LabVIEW control software was re-written to switch from
374 the Zeiss RemCon communication protocol to the Zeiss API which reduced the overhead by
375 several seconds per imaging/milling cycle.
376 The coated samples were imaged by a 0.14–0.3 nA electron beam with 0.7–1.2 keV
377 landing energy at 0.1–2 MHz. Detailed conditions are listed in Table 1. In most cases, both
378 backscattered and secondary electron signals were collected by InLens detector to provide

379 better signal-to-noise ratio. A faster SEM scanning rate was applied on samples with stronger
380 staining contrast thus larger imaging volumes were obtained. The x-y pixel size was set at 4 nm.
381 A subsequently applied focused Ga+ beam of 15 nA at 30 keV strafed across the top surface and
382 ablated away 4 nm of the surface. The newly exposed surface was then imaged again. The
383 ablation – imaging cycle continued for two to five weeks to complete FIB-SEM imaging one
384 sample. The sequence of acquired images formed a raw imaged volume, followed by post
385 processing of image registration and alignment using a Scale Invariant Feature Transform
386 (SIFT)[25] based algorithm to form isotropic 4 nm voxels. The final aligned stack consists of an
387 isotropic volume, containing multiple complete cells, which can be viewed in any arbitrary
388 orientations.

389 ## Evaluation of FIB-SEM resolution

390 In order to evaluate the actual resolution in the acquired FIB-SEM datasets we analyzed the
391 transitions of the edges of the ribosomes abundant within the cell volumes. Ribosomes are
392 macromolecular machines consisting of RNA and associated proteins. Their small size (20–30
393 nm), abundance in the cytoplasm of living cells, and the fact that they are stained with high EM
394 contrast makes them good candidates for resolution evaluation.

395 First, we selected volumes of approximately 1000–2000 x 1000 x 1000 pixels in cultured
396 datasets. These volumes were selected in the middle of datasets in areas with large number of
397 ribosomes. We then calculated histograms of grey level values in these volumes and subtracted
398 ~0.8 * histogram max to bring the average cytoplasmic material signal level close to 0. We then
399 used Laplacian of Gaussian (LoG) algorithm (part of Python scikit-image package). It computes
400 the Laplacian of Gaussian images with successively increasing standard deviation. We had set

401 the limit of standard deviation for LoG between 1 and 2.5 pixels (all these datasets have 4nm
402 voxels). Filters were used to exclude the following blobs: average value below zero, edge value
403 above 0.4 times of max value, 37%–63% transition longer than 15nm, amplitudes below certain
404 threshold so that at least approximately 3000 blobs per dataset were remaining for analysis.
405 The summaries of the 37%–63% transitions and 20%–80% transitions for the 3D
406 ribosome blobs selected in cultured cell datasets are plotted in Fig. 1b. The histograms of the
407 37%–63% transitions these datasets are shown in Extended Data Fig. 2. The examples of 3D
408 blobs for each dataset are presented in Extended Data Fig. 3–9. For each dataset the cross-
409 sections and transition analysis for 3 brightest and 3 dimmest blobs are shown.

410 ## Accurate determination of FIB-SEM milling rate

411 The position of a sample block face can be measured by the SEM beam and the FIB beam
412 independently. An in-line auto focus routine[6] keeps the SEM images in focus throughout the
413 entire image acquisition. While the working distance of the SEM beam detects the block face
414 position by measuring its distance from the SEM objective lens, the FIB milling position under
415 closed-loop control indicates the block face position directly from the orthogonal angle. As the
416 sample block face being imaged then milled away layer-by-layer, the SEM working distance and
417 the FIB beam position track the block face location accordingly. Therefore, one can estimate the
418 total thickness milled away by FIB based on the changes of either SEM working distance or FIB
419 milling position from the beginning to the end of the FIB-SEM acquisition. The average milling
420 rate of z-step can then be calculated as the total milling depth divided by the number of image
421 frames. Here we report the average z-scaling factors derived from the two measurement
422 approaches in Extended Data Table 1. It can be used to scale the dataset to generate real

423 isotropic voxels. For example, HeLa Cell 2017-06 dataset has a z-scaling factor of 1.31 which

424 means the actual z-step is average at 5.2 nm instead of 4.0 nm.

425 Data availability

426 All raw and segmented datasets in this work are available on OpenOrganelle website

427 (https://openorganelle.janelia.org).

428 Code availability

429 FIB-SEM image acquisition LabVIEW codes used in this work are available from

430 https://doi.org/10.7554/eLife.25916.031.

Acknowledgements

We thank K. Hayworth and W. Qiu at Howard Hughes Medical Institute (HHMI) Janelia Research Campus (JRC) for invaluable discussions and data collection support. We gratefully acknowledge P. Rivlin, S. Plaza, and I. Meinertzhagen for JRC EM shared resource and FlyEM project team support on staining protocols development. We thank the electron microscopy facility of MPI-CBG and of the CMCB Technology Platform at TU Dresden for their services. We also thank Y. Wu from Pietro De Camilli's laboratory at Yale for advice.

Funding

C.S.X., S.P., G.S., D.B., S.T., Z.L., A.V.W., H.A.P., N.I., T.C.W., H.F.H. are funded by Howard Hughes Medical Institute (HHMI). A.M. received support from the Carl Gustav Carus Faculty of Medicine at TU Dresden via a MeDDrive GRANT. A.M. and M.S. were supported with funds from the German Center for Diabetes Research (DZD e.V.) by the German Ministry for Education and Research (BMBF), from the Germain-Israeli Foundation for Scientific Research and Development (GIF) (grant I-1429-201.2/2017), from the German Research Foundation (DFG) jointly with the Agence nationale de la recherche (ANR) (grant SO 818/6-1) to M.S.. H.K.H and S.B.v.E. are funded by NIAID grant R01AI138625. R.V.F. is supported by NIH R01GM124348. T.C.W. is supported by NIH R01GM097194. J.C. is a fellow of the Damon Runyon Cancer Research Foundation.

449 ## Author Contributions

450 C.S.X. and H.F.H. supervised the project; C.S.X., S.P., G.S., and H.F.H. wrote the manuscript with
451 input from all co-authors; C.S.X. developed enhanced FIB-SEM platform for large volume high
452 resolution imaging, and optimized imaging conditions; C.S.X., S.P., and G.S. conducted FIB-SEM
453 experiments; C.S.X. and S.P. performed image post processing; S.P., G.S., A.M., A.T.R., H.K.H.,
454 S.B.v.E., Z.L., A.V.W., H.A.P., N.I., and J.C. prepared samples; G.S., A.M., A.T.R., and S.T. analyzed
455 data; D.B. prepared and uploaded data to OpenOrganelle website; T.C.W., R.V.F., S.B.v.E., I.M.,
456 and M.S. proposed biological questions and provided samples.

457 ## Competing interests

458 Portions of the technology described herein are covered by U.S. Patent 10,600,615 issued to
459 C.S.X. and H.F.H., and assigned to HHMI.

Figures

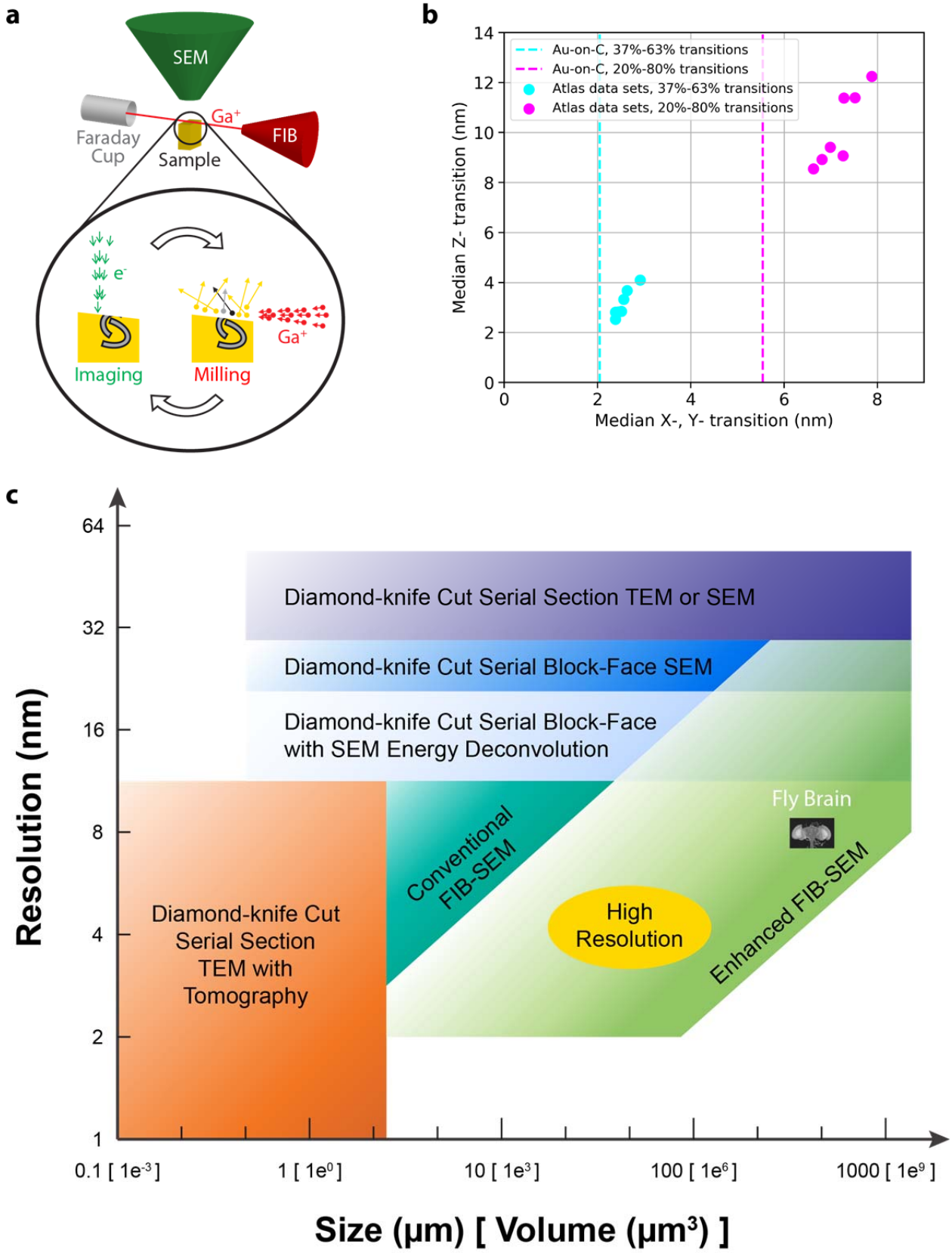
a
SEM
Faraday Cup
Ga+
FIB
Sample
e-
Imaging
Milling
Ga+
b
Au-on-C, 37%-63% transitions
Au-on-C, 20%-80% transitions
Atlas data sets, 37%-63% transitions
Atlas data sets, 20%-80% transitions
Median Z- transition (nm)
Median X-, Y- transition (nm)
c
Diamond-knife Cut Serial Section TEM or SEM
Diamond-knife Cut Serial Block-Face SEM
Diamond-knife Cut Serial Block-Face with SEM Energy Deconvolution
Conventional FIB-SEM
Fly Brain
High Resolution
Enhanced FIB-SEM
Diamond-knife Cut Serial Section TEM with Tomography
Resolution (nm)
Size (µm) [Volume (µm³)]
0.1 [1e-3]
1 [1e0]
10 [1e3]
100 [1e6]
1000 [1e9]

461

462 Fig. 1 **Enhanced FIB-SEM configuration, operation, resolution, and volume**. **a**, Sketch of FIB
463 ablation and SEM imaging. The two operations iterate every minute and repeat tens of
464 thousands of times to make 3D image stacks, **b**, Resolution characterization: X position of
465 vertical line indicates the step edge transition as observed on gold nano particles on a carbon
466 substrate, the round dots are step edge transitions on ribosomes along x-y axis and the z axis.
467 Each dot represents the average value from more than 3000 ribosomes in one of the seven
468 cultured cell samples. **c**, Smallest isotropic voxel size vs volume for comparing different volume
469 EM methods. The light green space indicates the new Resolution-Volume regime uniquely
470 accessible with enhanced FIB-SEM technology through long term imaging. The regime of this
471 work at 4 nm isotropic voxel sampling is highlighted in yellow.

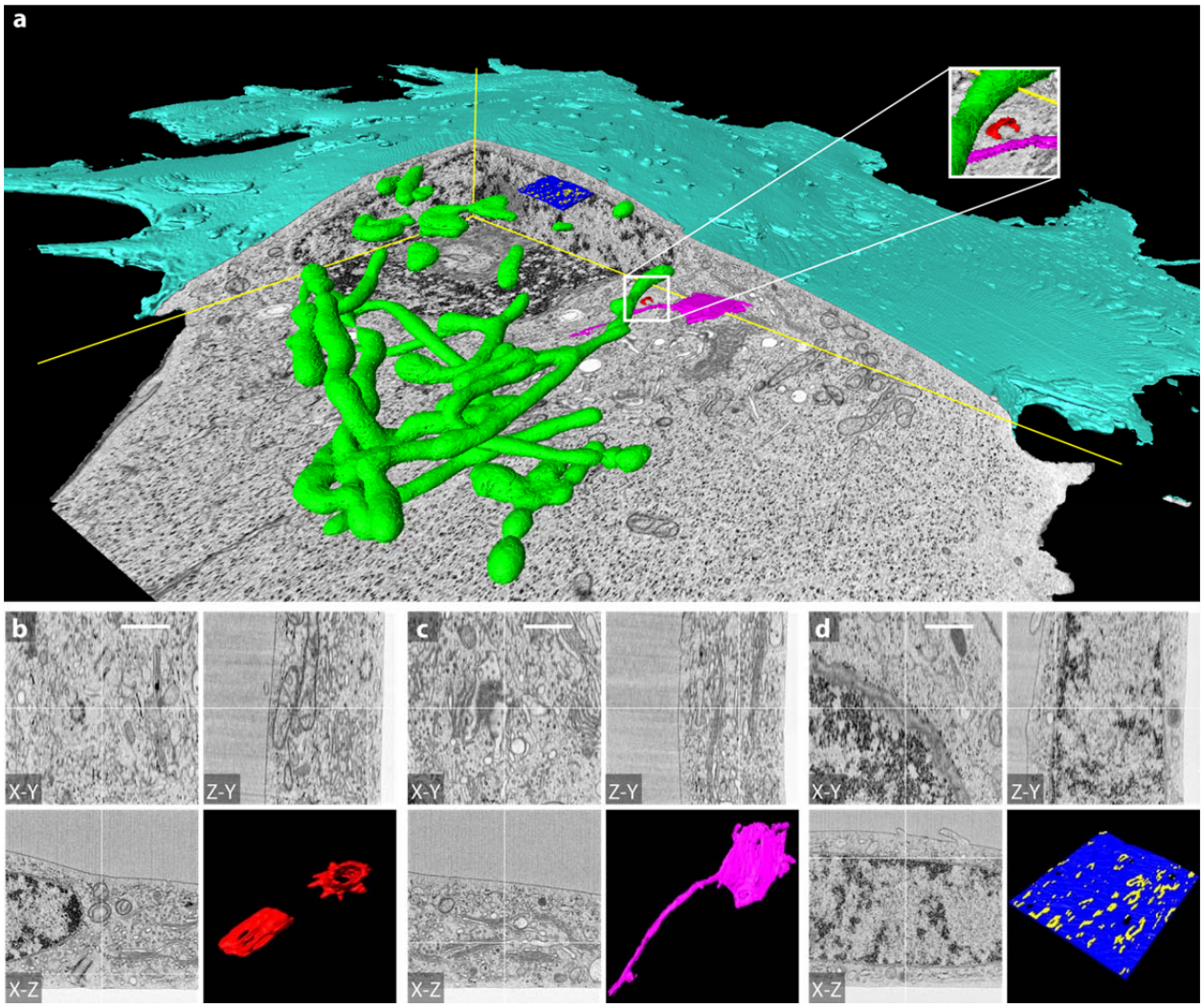

Fig. 2 **Interphase HeLa cell**. **a**, FIB-SEM overview with cutaway, and manually segmented interior features (mitochondria, green; centrosomes, red; one cistern of a Golgi stack, magenta; a segment of nuclear membrane, blue, polyribosome chains, yellow). Zoomed in cross-sections of three select areas containing, **b**, Centrosomes, **c**, Golgi stack, and **d**, Nucleus. Scale bars are 1 µm.

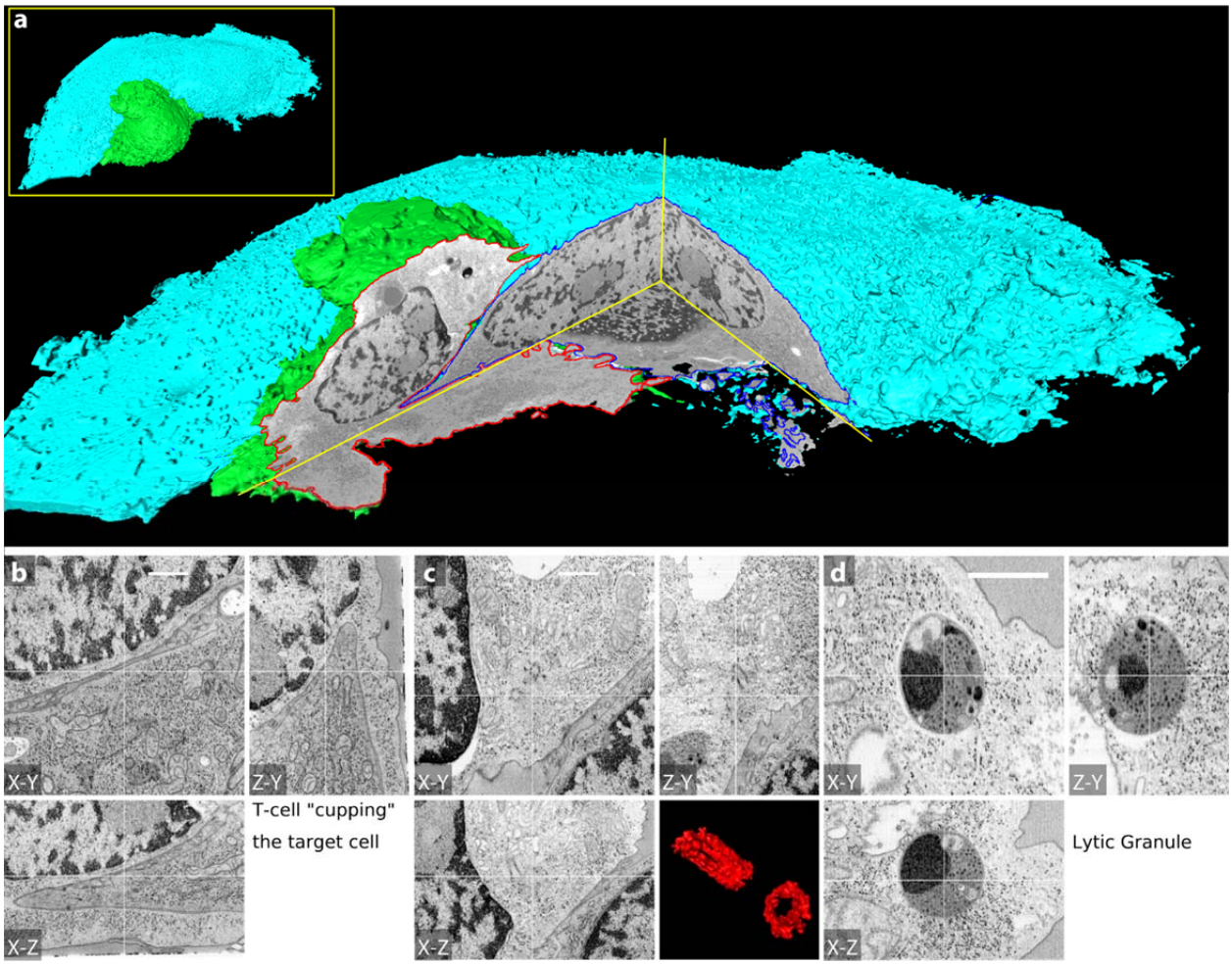

Fig. 3 **Murine CTL engaging an ovarian cancer cell**. **a,** FIB-SEM overview with cutaway, and manually segmented membranes of CTL (green surface and red contour) and cancer cell (cyan surface and blue contour). Zoomed in cross-sections of three select areas containing **b**, CTL cell cupping the target cancer cell, **c,** Centrosome, and **d**, Lytic granule. Scale bars are 1 µm.

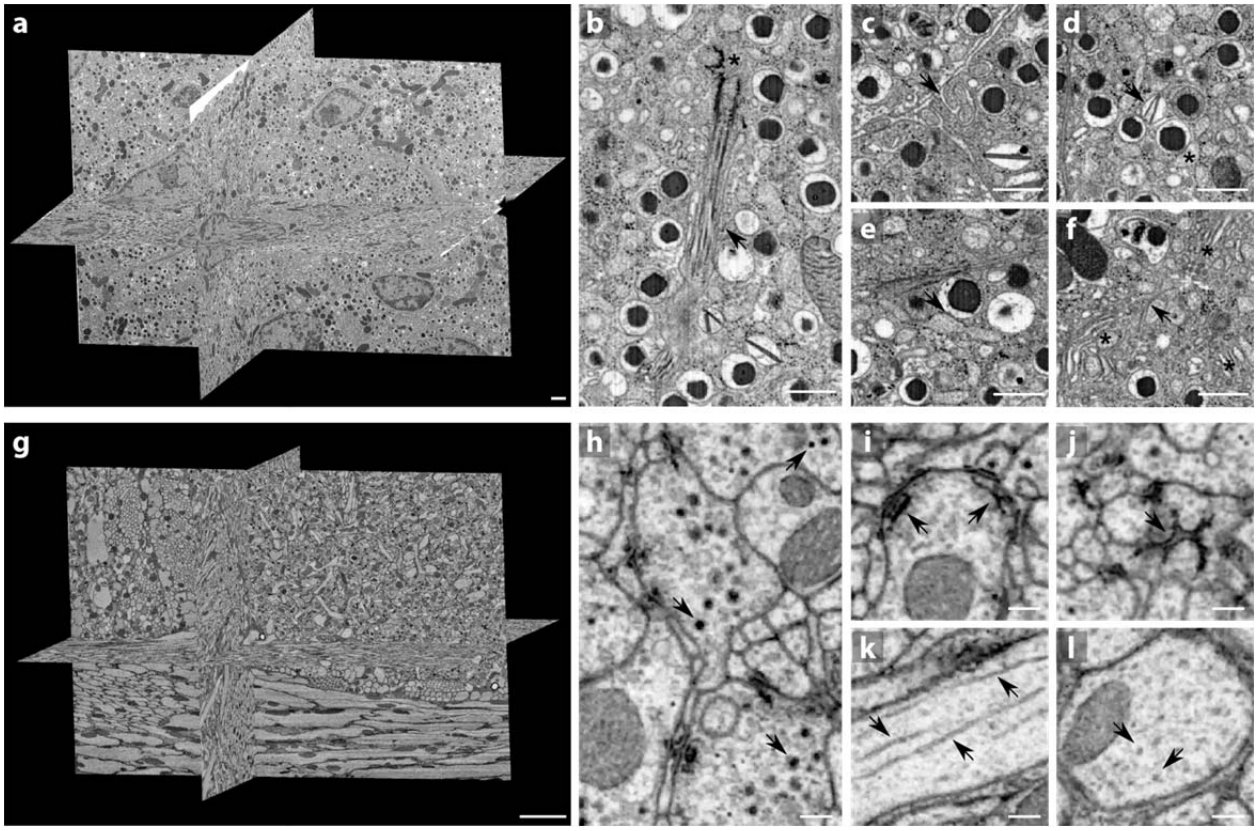

Fig. 4 **Tissue sample datasets**. **a**, Pancreatic islets treated with 16.7 mM glucose containing several complete beta cells with detailed structures shown in **b**, A primary cilium with axoneme (arrow) and centrioles (asterisk), **c**, Intermingled microvilli (arrow), **d**, Ultrastructural diversity among insulin SGs containing rod-shaped (arrow) or spherical crystals (asterisk), **e**, Contacts of ER and insulin SGs (arrow), **f**, Microtubules (arrow), Golgi apparatus (asterisks) and ribosomes. **g**, *Drosophila* fan-shaped body with detailed structures shown in **h**, Dense-core vesicles of different sizes (arrows), **i**, Multiple synaptic sites viewed from the side (arrows), **j**, A presynaptic T-bar viewed from the top (arrow), **k**, A longitudinal-section view of microtubules (arrows), **l**, A cross-section view of microtubule arrays (arrows). Scale bar, 1 µm in **a**, 500 nm in **b–f**, 5 µm in **g**, 200 nm in **h–l**.

494 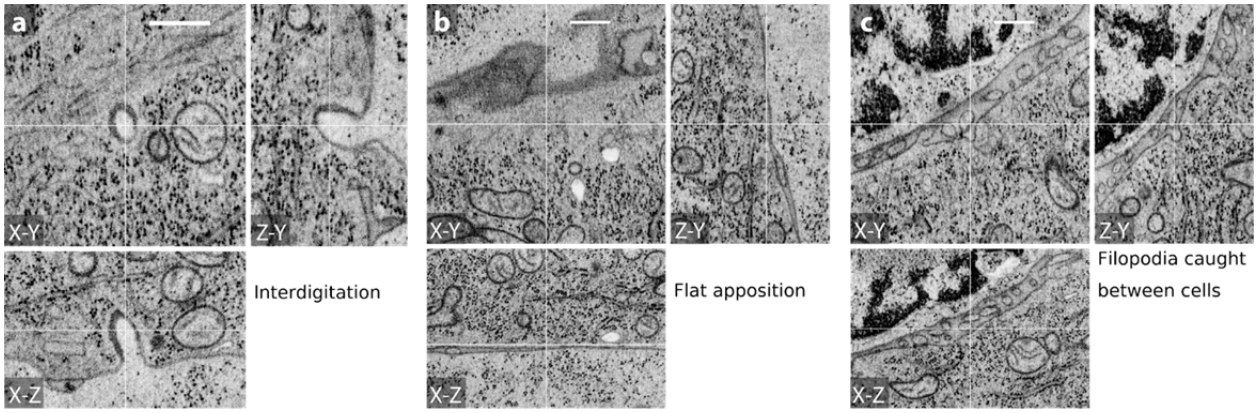

495 Extended Data Fig. 1 **Murine CTL engaging an ovarian cancer cell.** Zooms on regions showing

496 different synapse topology features. **a**, Interdigitation, **b**, Flat apposition, and **c**, Filopodia

497 caught between cells. Scale bars are 0.5 µm.

a

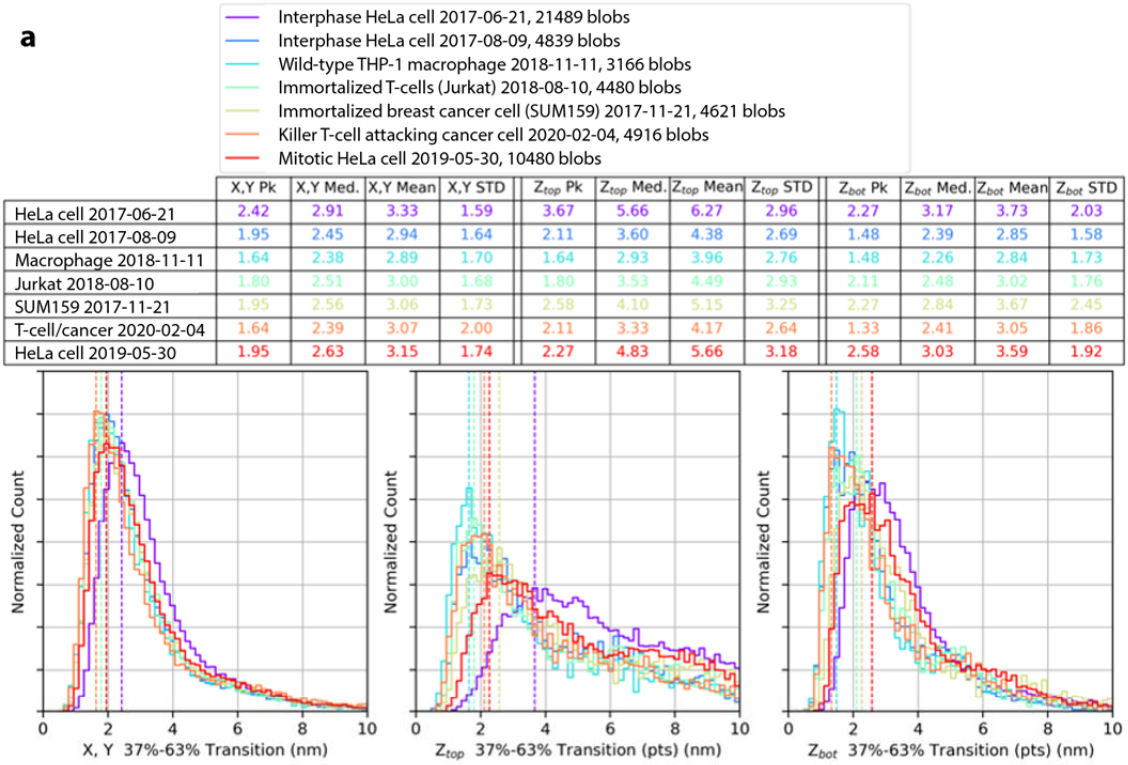

	X,Y Pk	X,Y Med.	X,Y Mean	X,Y STD	Z_{top} Pk	Z_{top} Med.	Z_{top} Mean	Z_{top} STD	Z_{bot} Pk	Z_{bot} Med.	Z_{bot} Mean	Z_{bot} STD
HeLa cell 2017-06-21	2.42	2.91	3.33	1.59	3.67	5.66	6.27	2.96	2.27	3.17	3.73	2.03
HeLa cell 2017-08-09	1.95	2.45	2.94	1.64	2.11	3.60	4.38	2.69	1.48	2.39	2.85	1.58
Macrophage 2018-11-11	1.64	2.38	2.89	1.70	1.64	2.93	3.96	2.76	1.48	2.26	2.84	1.73
Jurkat 2018-08-10	1.80	2.51	3.00	1.68	1.80	3.53	4.49	2.93	2.11	2.48	3.02	1.76
SUM159 2017-11-21	1.95	2.56	3.06	1.73	2.58	4.10	5.15	3.25	2.27	2.84	3.67	2.45
T-cell/cancer 2020-02-04	1.64	2.39	3.07	2.00	2.11	3.33	4.17	2.64	1.33	2.41	3.05	1.86
HeLa cell 2019-05-30	1.95	2.63	3.15	1.74	2.27	4.83	5.66	3.18	2.58	3.03	3.59	1.92

b

	X,Y Pk	X,Y Med.	X,Y Mean	X,Y STD	Z_{top} Pk	Z_{top} Med.	Z_{top} Mean	Z_{top} STD	Z_{bot} Pk	Z_{bot} Med.	Z_{bot} Mean	Z_{bot} STD
HeLa cell 2017-06-21	6.33	7.88	8.31	2.94	15.70	15.44	15.48	4.54	7.27	8.97	9.71	3.88
HeLa cell 2017-08-09	5.39	6.81	7.43	3.15	12.89	11.40	11.13	3.54	7.27	7.20	7.22	2.46
Macrophage 2018-11-11	5.39	6.63	7.27	3.28	13.36	10.97	10.78	4.18	7.27	7.05	7.13	2.73
Jurkat 2018-08-10	5.39	6.99	7.56	3.19	14.30	12.29	11.91	4.03	7.27	7.56	7.65	2.77
SUM159 2017-11-21	5.86	7.28	7.79	3.33	15.23	13.93	13.69	5.24	5.86	9.21	9.67	4.37
T-cell/cancer 2020-02-04	4.92	7.26	7.87	3.69	11.48	10.84	10.74	3.82	8.20	7.80	7.82	3.76
HeLa cell 2019-05-30	5.39	7.52	7.99	3.24	14.30	14.55	14.36	4.26	8.67	9.06	9.15	3.14

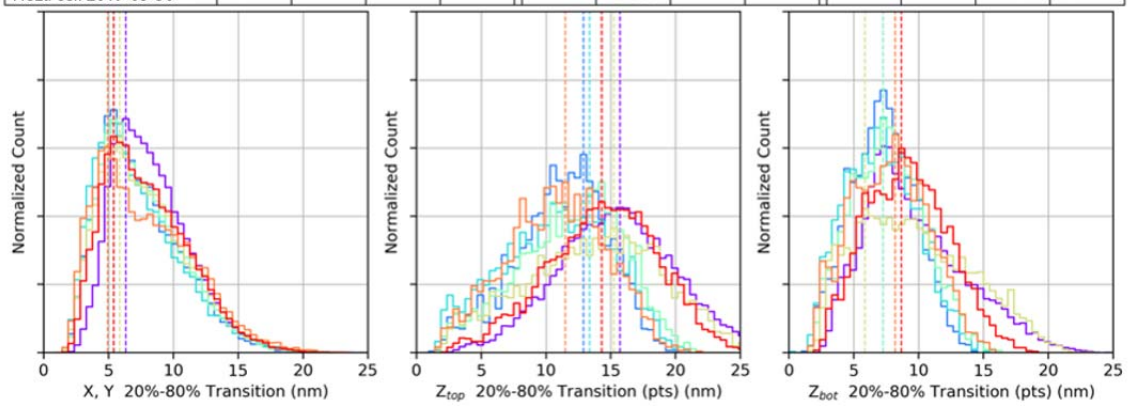

Extended Data Fig. 2 **Edge transition distributions determined from ribosomes in cultured cells datasets**. Distributions of 37%–63% (**a**) and 20%–80% (**b**) transition distances in X-, Y- (left), Z_{top}- (center), and Z_{bot}- (right) directions.

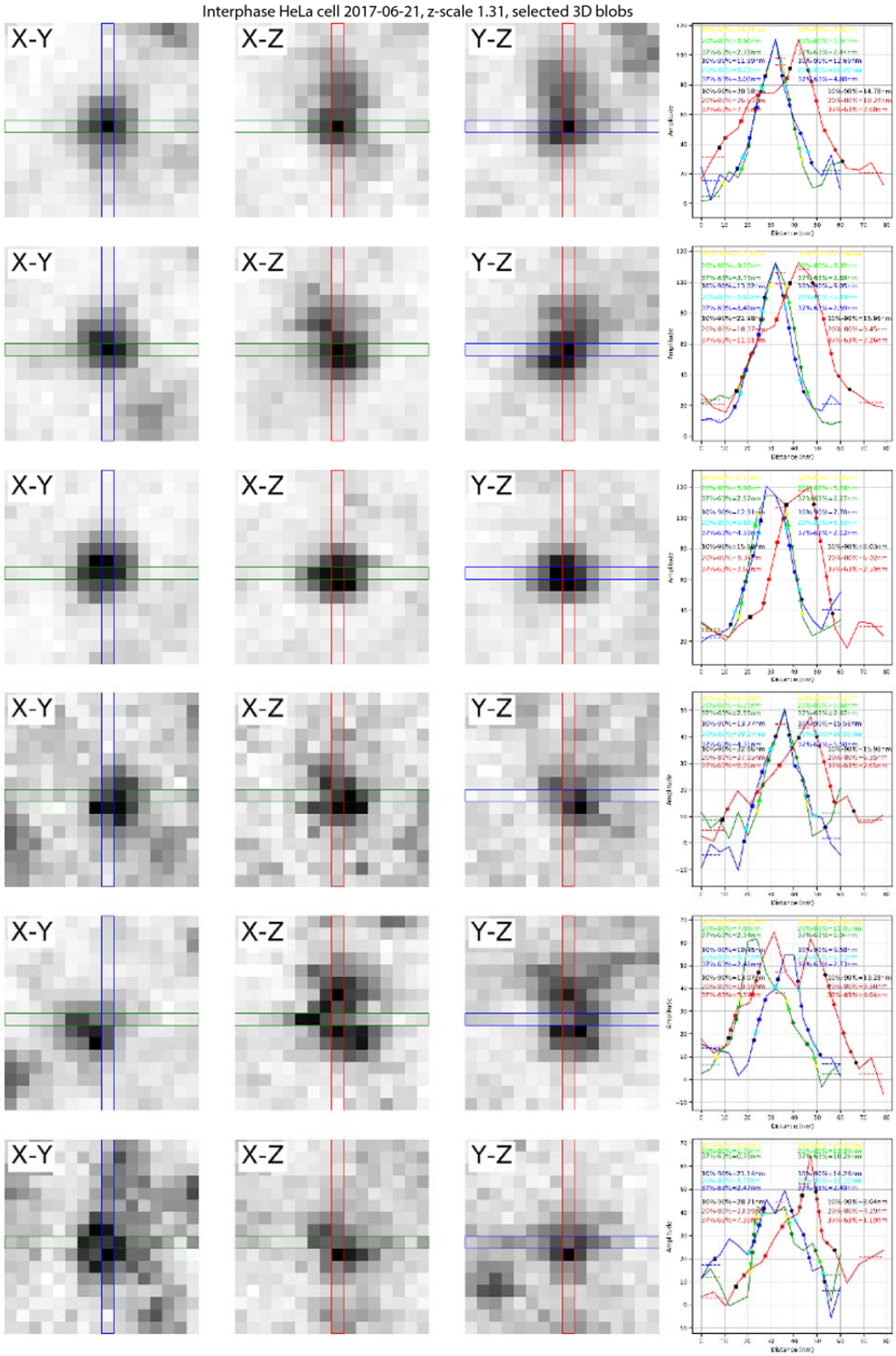

Extended Data Fig. 3 **Cross-sections of the example of ribosomes from the dataset HeLa Cell2 and the profiles with the transition analysis.**

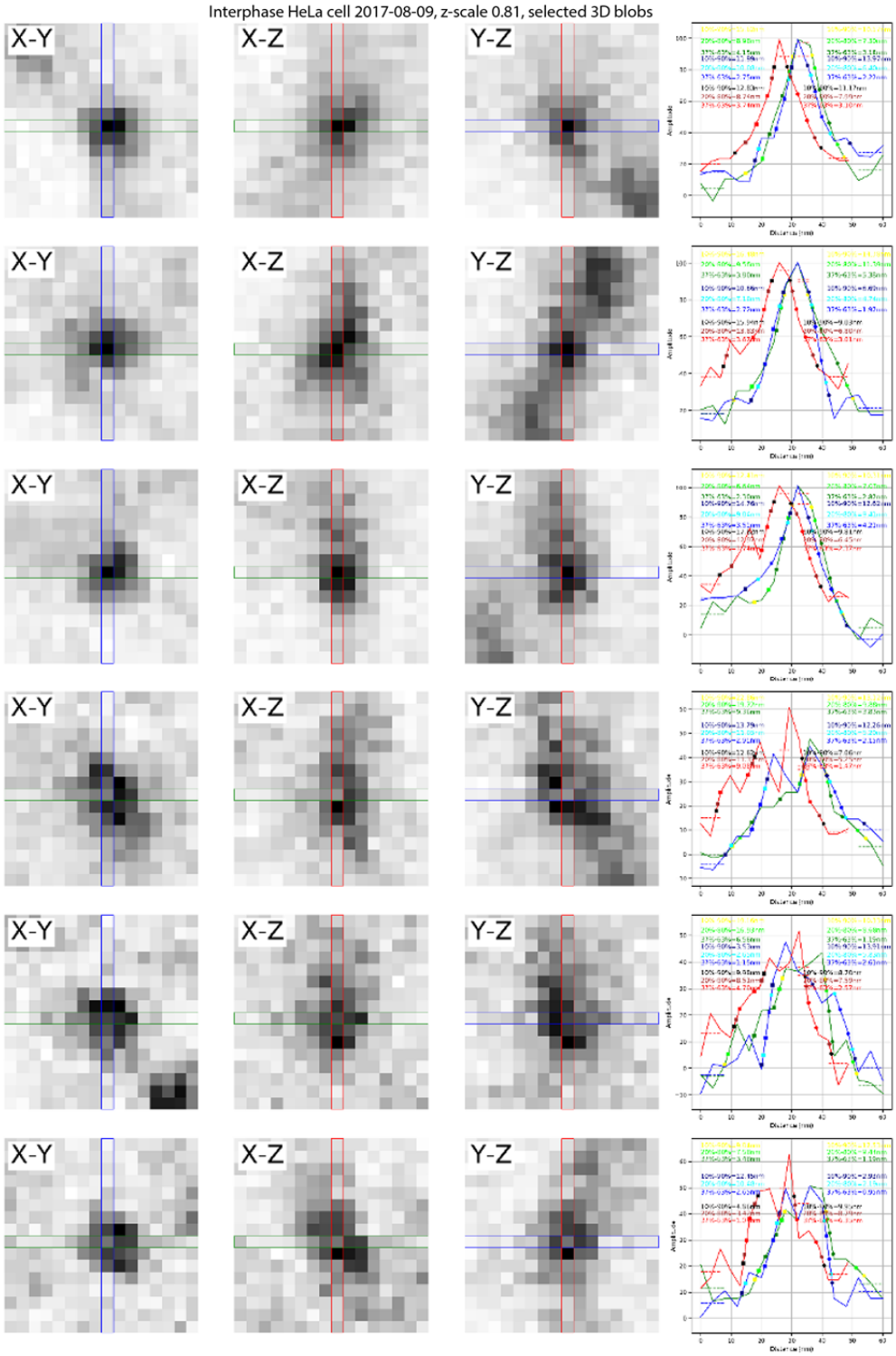

Extended Data Fig. 4 **Cross-sections of the example of ribosomes from the dataset HeLa Cell3 and the profiles with the transition analysis.**

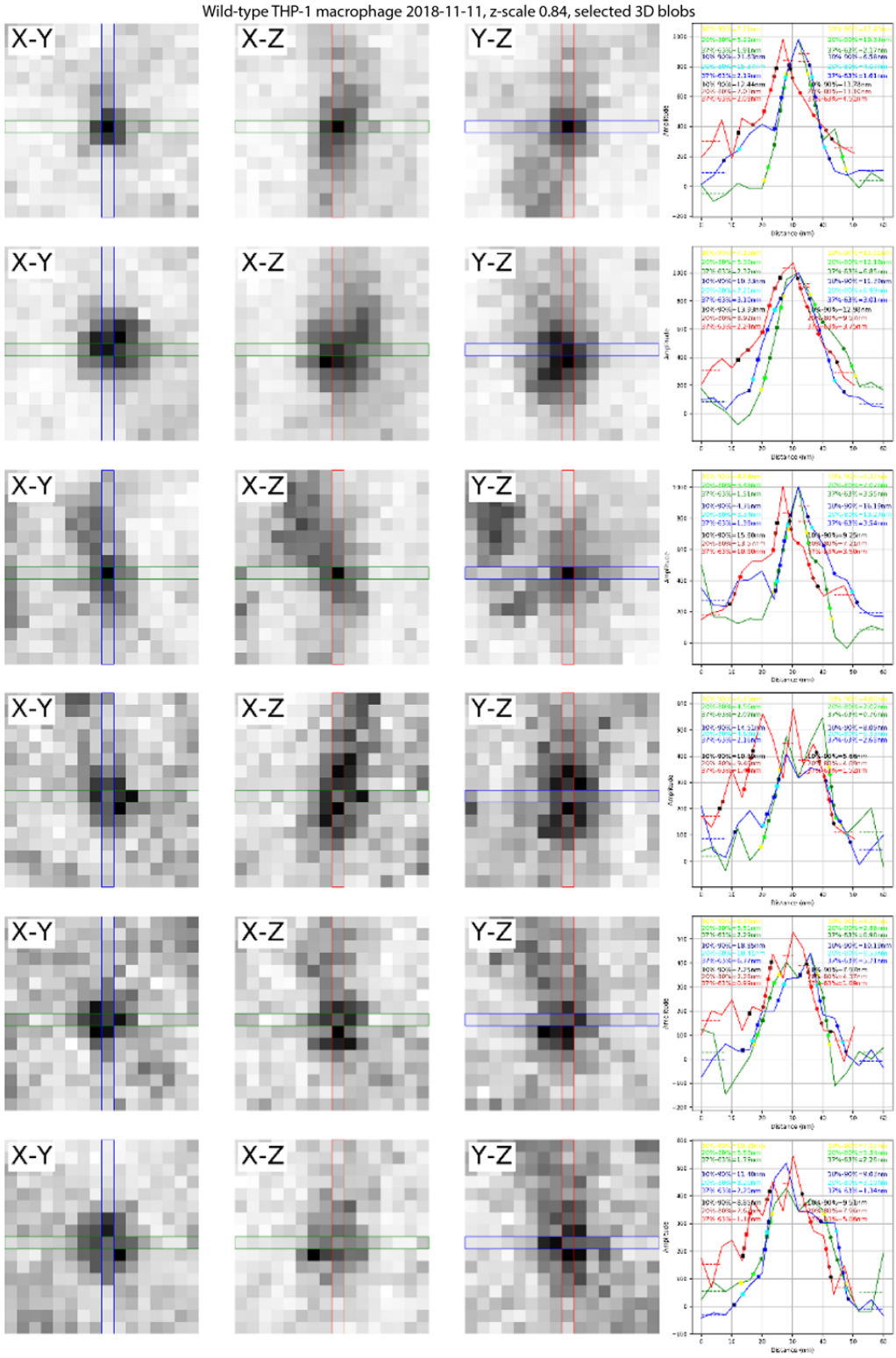

Extended Data Fig. 5 **Cross-sections of the example of ribosomes from the dataset Macrophage Cell2 and the profiles with the transition analysis.**

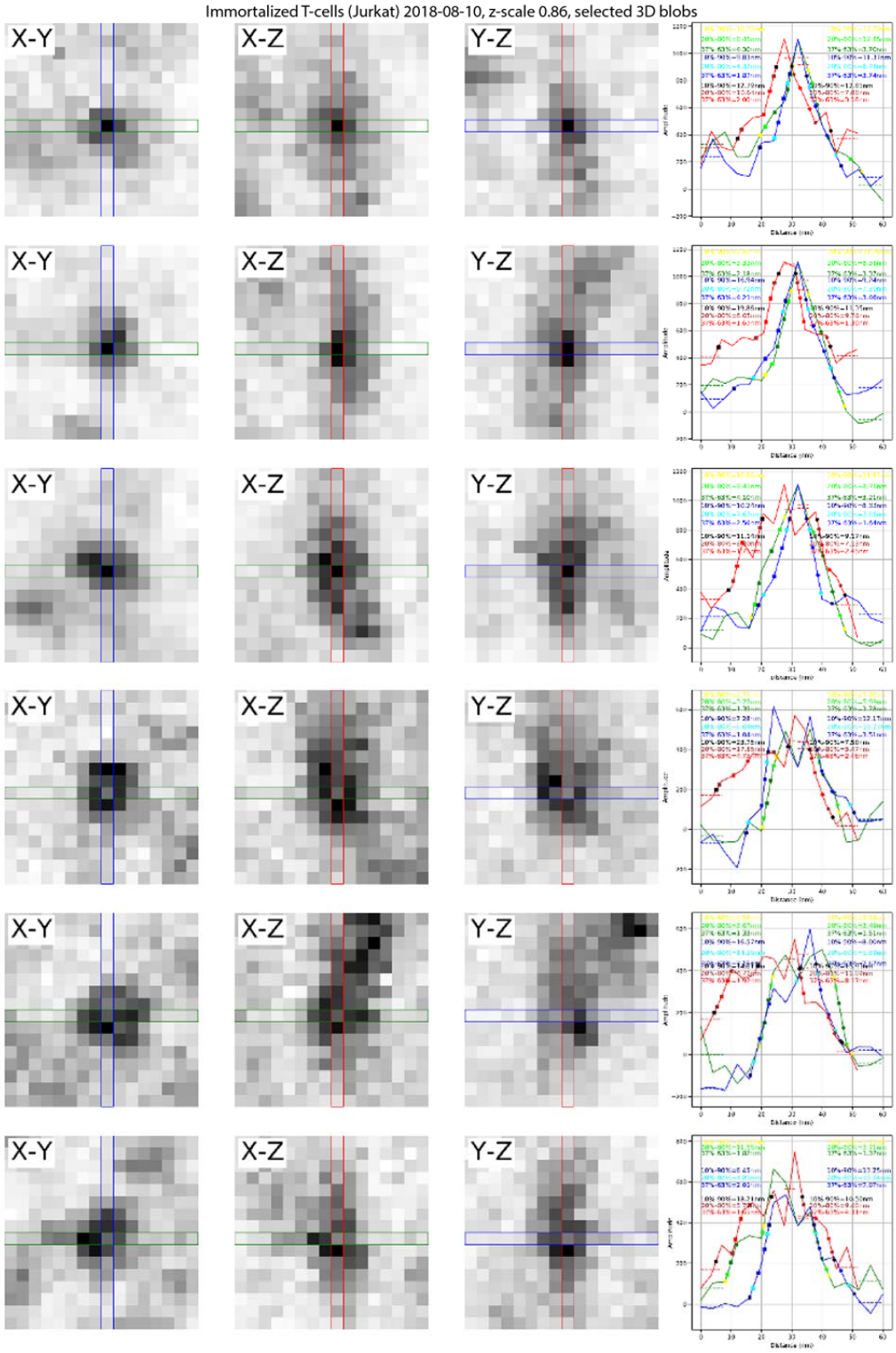

Extended Data Fig. 6 **Cross-sections of the example of ribosomes from the dataset Jurkat Cell1 and the profiles with the transition analysis.**

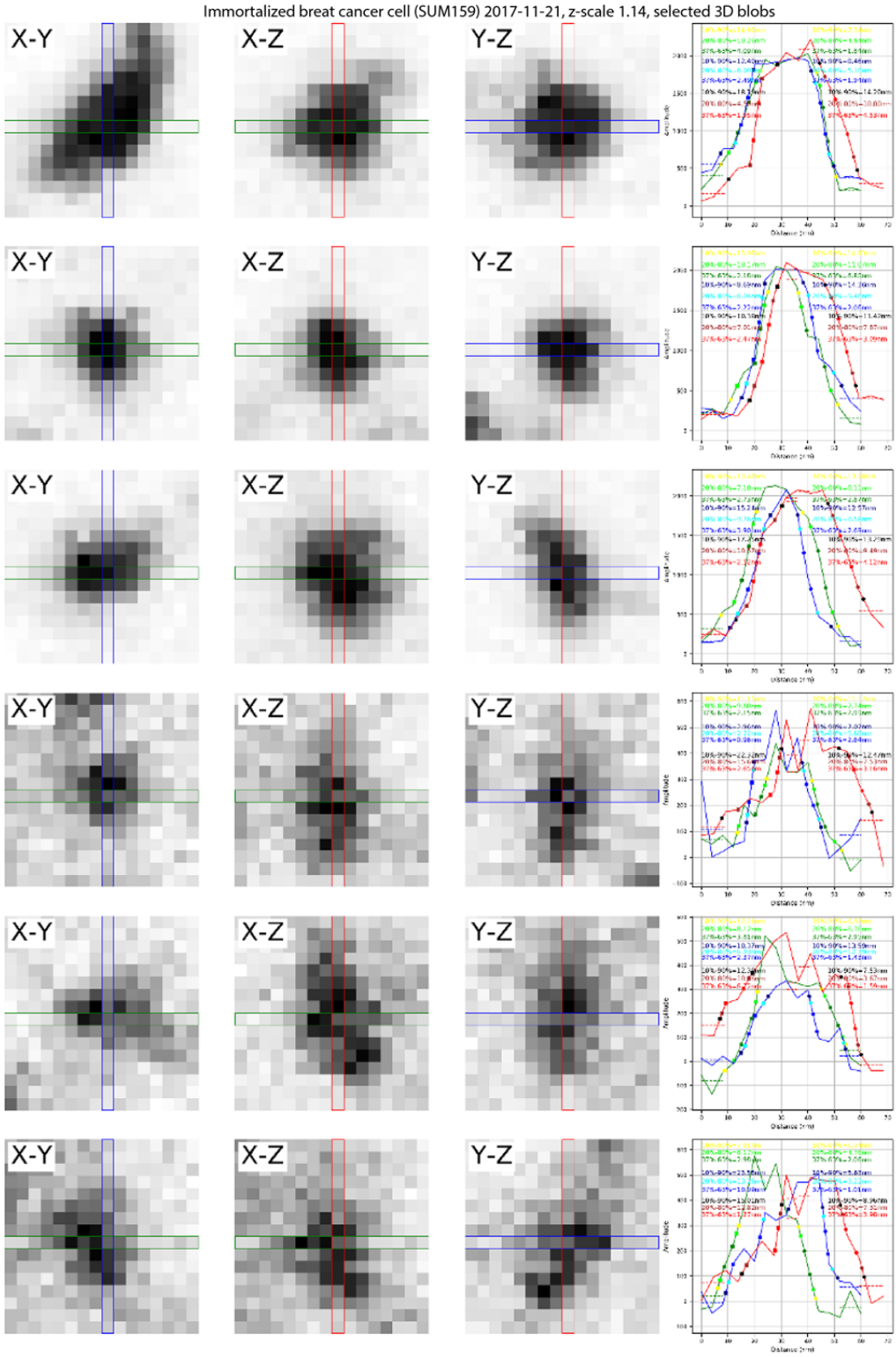

514

515 Extended Data Fig. 7 **Cross-sections of the example of ribosomes from the dataset SUM159**

516 **Cell2 and the profiles with the transition analysis.**

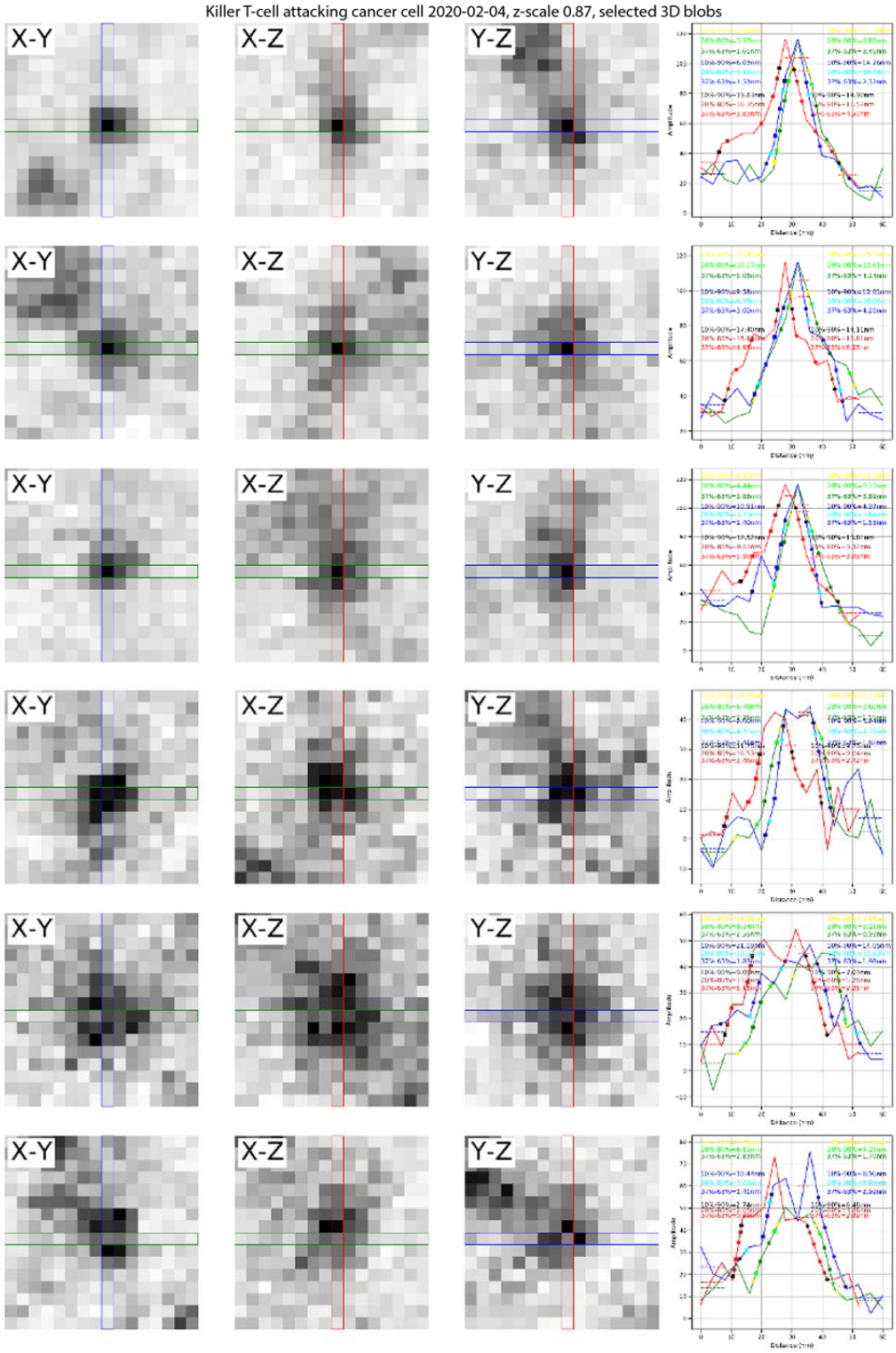

Extended Data Fig. 8 **Cross-sections of the example of ribosomes from the dataset T-Cell on Cancer Cell and the profiles with the transition analysis.**

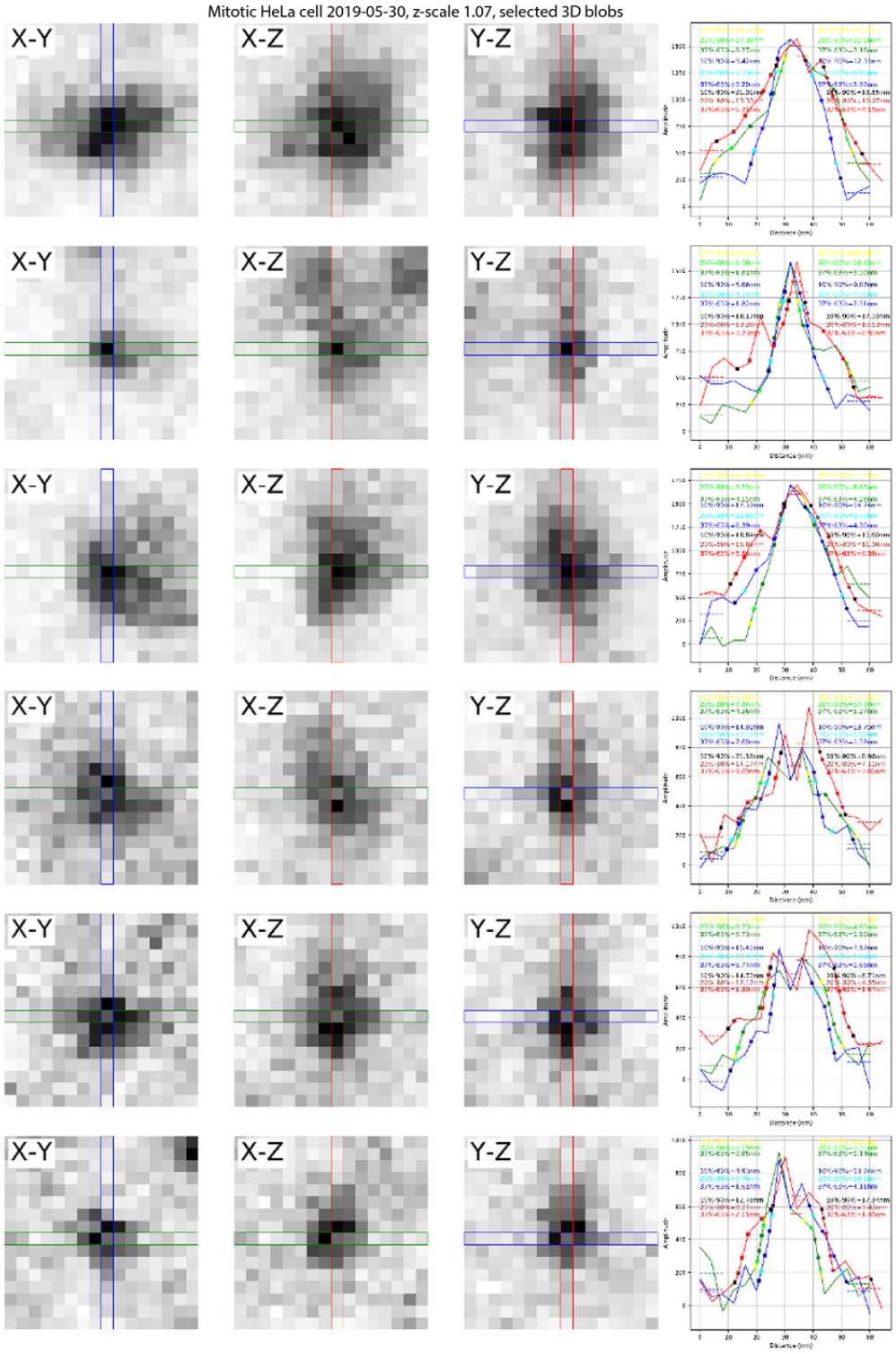

Extended Data Fig. 9 **Cross-sections of the example of ribosomes from the dataset HeLa Cell4 and the profiles with the transition analysis.**

Tables

Table 1. Descriptions of exemplary datasets with selected imaging conditions

Sample Description	Protocol	Landing Energy (kV)	Imaging Current (nA)	Scan Speed (MHz)	Acquisition Duration (days)	Data Volume: X * Y * Z (μm^3)	Z-scaling factor
Cell 4 nm							
Interphase HeLa cell 2017-06-21	High pressure freezing, freeze-substitution with 2% OsO4 0.1% UA 3% H2O in Acetone, resin embedding in Eponate 12	0.9	0.24	0.1	25	48 * 6 * 25 (7800)	1.31
Interphase HeLa cell 2017-08-09†		1.0	0.24	0.2	31	50 * 4 * 48 (9600)	0.81
Mitotic HeLa cell 2019-05-30		0.9	0.24	0.2	15	30 * 14 * 33 (13300)	1.07
Wild-type THP-1 macrophage 2018-11-11		1.2	0.24	0.2	20	40 * 8 * 44 (14200)	0.84
Immortalized T-cells (Jurkat) 2018-08-10		1.0	0.24	0.2	19	40 * 12 * 34 (16400)	0.86
Immortalized breast cancer cell (SUM159) 2017-11-21‡		1.2	0.24	0.2	19	64 * 11 * 31 (21900)	1.14
Killer T-Cell attacking cancer cell 2020-02-04†		0.7	0.25	0.2	29	74 * 13 * 48 (45500)	0.87
Tissue 4 nm							
Isolated murine pancreatic islets 2019-03-01†	HPF, FS with 2%OsO4, 1% UA, 0.5% GA, 5% H2O in Acetone with 1% Methanol followed by 0.2% TCH in 80% Methanol at RT, 2% OsO4 in Acetone at RT, 1% UA in Acetone + 10% Methanol	0.9	0.14	0.2	15	30 * 20 * 29 (17400)	0.85
Drosophila brain: Fan-shaped body of a 5-day-old male adult 2019-09-14†	Chemical Fixation, ORTO-Lead-EPTA staining via Progressive Lowering of Temperature and Low Temperature Staining (PLT-LTS) heavy metal enhancement protocol	0.7	0.24	1.5	15	45 * 56 * 45 (113400)	1
Drosophila brain: Accessory calyx of a 5-day-old male adult 2019-12-06		0.7	0.3	2	19	50 * 40 * 87 (175000)	0.93

† Figures in main text.

‡ Treated with 0.5 mM oleic acid for 45 mins prior to high pressure freezing to induce the formation of lipid droplets.

529 Extended Data Table 1. Z scaling factors estimated using SEM working distance and FIB milling

530 voltage.

DataSet	Z (milling direction) pixel scaling factor		
	SEM Working Distance (WD)	**FIB milling voltage (MV)**	**Mean (WD, MV)**
Interphase HeLa cell 2017-06-21	1.22	1.40	1.31
Interphase HeLa cell 2017-08-09	0.80	0.83	0.81
Mitotic HeLa cell 2019-05-30	1.07	1.07	1.07
Wild-type THP-1 macrophage 2018-11-11	0.81	0.87	0.84
Immortalized T-cells (Jurkat) 2018-08-10	0.84	0.88	0.86
Immortalized breast cancer cell (SUM159) 2017-11-21	1.13	1.14	1.14
Killer T-Cell attacking cancer cell 2020-02-04	0.88	0.87	0.87
Isolated murine pancreatic islets 2019-03-01	0.86	0.84	0.85
Drosophila Fan-shaped body 2019-09-14	0.98	1.03	1.00
Drosophila Accessory calyx 2019-12-06	0.95	0.92	0.93

531

532 ## References

[20] Sartori, N., Richter, K., & Dubochet, J. Vitrification depth can be increased more than 10-fold by high-pressure freezing. *J. Microsc.* **172**(1), 55–61 (1993). https://doi.org/10.1111/j.1365-2818.1993.tb03393.x

[21] Gotoh M., Maki T., Kiyoizumi T., Satomi S., & Monaco A. P. An improved method for isolation of mouse pancreatic islets. *Transplantation* **40**, 437–438 (1985). https://doi.org/ 10.1097/00007890-198510000-00018

[22] Müller, A. et al. A global approach for quantitative super resolution and electron microscopy on cryo and epoxy sections using self-labeling protein tags. *Sci. Rep.* **7**, 23 (2017). https://doi.org/10.1038/s41598-017-00033-x

[23] Kremer, J. R., Mastronarde, D. N., & McIntosh, J. R., Computer visualization of three-dimensional image data using IMOD. *J. Struct. Biol.* **116**, 71–76 (1996). https://doi.org/10.1006/jsbi.1996.0013

[24] Lu Z. et al. En bloc preparation of *Drosophila* brains enables high-throughput FIB-SEM connectomics. *bioRxiv*: 855130 (2019). https://doi.org/10.1101/855130

[25] Saalfeld, S., Cardona, A., Hartenstein, V. & Tomančák, P. As-rigid-as-possible mosaicking and serial section registration of large ssTEM datasets. *Bioinformatics* **26**, i57–63 (2010). https://doi.org/10.1093/bioinformatics/btq219